ACES Asian Chemical Editorial Society

doi.org/10.1002/cnma.202200469

CHEMNANOMAT
Research Article

www.chemnanomat.org

Simple Fabrication of ε-Fe_2O_3 Nanoparticles Containing Silica Monoliths with Enhanced Coercivity

Laura Altenschmidt,[a] Patricia Beaunier,[b] Amélie Bordage,[a] Eric Rivière,[a] Giulia Fornasieri,[a] and Anne Bleuzen*[a]

Abstract: Most of large-size permanent room-temperature hard magnets contain rare-earth elements. Here, we present the preparation of a large-size rare-earth free hard magnet based on the loading of the ordered mesoporosity of a preformed ordered mesoporous silica monolith obtained by a sol-gel route with the $Fe(NO_3)_3$ salt, followed by a simple calcination in air. The investigation of the influence of the thermal treatment temperature as well as the Fe/Si ratio on the microstructure of the ε-Fe_2O_3/SiO_2 nanocomposites reveals well-controlled ε-Fe_2O_3 particles size and size distribution. Their magnetic study allows us i) to specify the size of the particles with an enhanced coercivity and ii) to show a linear correlation between the magnetic coercivity of the materials and the mass percent of these particles in the nanocomposites. A ε-Fe_2O_3 based bulk hard magnet with the highest coercive field of 18 kOe at room temperature was obtained by this synthesis process.

Introduction

Hard magnets are strategic components for large-scale fabrication of materials, which can find applications in many fields including electric motors, information storage and medicine.[1–3] The hard magnets the most currently used are rare-earth[2] (NdFeB, SmCo) and precious metal[4,5] (Pt or Pd) based compounds. Their drawbacks, that are high environmental cost for the former and high cost for the latter, have stimulated research for magnets made of earth-abundant and environmentally friendly elements, among them iron oxides. Thus, the ε-Fe_2O_3 phase has gained a lot of attention in the recent years due to the evidence of a large coercive field of up to 20 kOe at room temperature,[6–11] opening new perspectives in terms of cheap hard magnets made of earth-abundant elements. Interestingly, it was also shown that partial substitution of Fe ions in the ε-Fe_2O_3 phase affords the preparation of tunable electromagnetic wave absorbers over a wide frequency range up to 190 GHz[12,13] and of materials with an even higher coercivity[14] (35 kOe at room temperature) or with multiferroic properties.[15]

Iron(III) oxides exist in various polymorphic forms such as the most common hematite (α-Fe_2O_3) and maghemite (γ-Fe_2O_3) phases, as well as the rarer β-Fe_2O_3 and ε-Fe_2O_3 phases. The ε-Fe_2O_3 phase is not easy to obtain, since it appears in certain specific conditions as an intermediate between the γ-Fe_2O_3 and α-Fe_2O_3 phases, and is thus often polluted with one of these phases. In general, a stabilization of the ε-Fe_2O_3 phase can be achieved through a restriction of the reaction volume and fast reaction kinetics.[8] Thus, this oxide phase is exclusively prepared as a nanomaterial, generally through complex synthetic routes with a precise control of both the temperature of formation[16–18] and the size of the particles.[16,19–21] Using a porous silica matrix acting as an anti-sintering agent proved to be a very efficient way to prevent the agglomeration of the iron oxide particles and allows for the stabilization of the ε-Fe_2O_3 phase while preventing the formation of the thermodynamically stable α-Fe_2O_3 phase.[22] The choice of the precursor also influences the formation conditions of the ε-Fe_2O_3 phase. Typically, different iron salts are used as precursors, which are thermally decomposed in air and thereby transformed into an iron oxide. The most common salt precursors include iron nitrates and iron sulfates.[8,17,18,23] However, it is also possible to directly use γ-Fe_2O_3 nanoparticles and thermally treat them, inducing their transformation into the ε-Fe_2O_3 phase.[24,25] It could also be shown that the addition of alkaline earth metal ions, such as Ca^{2+}, Sr^{2+} or Ba^{2+}, in the synthesis medium favors the stabilization of the ε-Fe_2O_3 phase and induces a morphology change of the formed nanoparticles from spherical to rod-like.[19,26–29]

Besides the difficulties to obtain the pure ε-Fe_2O_3 phase, the crystal structure is not solely responsible for the magnetic properties. The magnetic behavior also depends on the particle size. It has been shown that the coercive field increases with increasing the average particle diameter but that, despite having the ε-Fe_2O_3 structure, particles with a size below 7.5 nm are superparamagnetic.[9] Also, the enhanced coercivity is only reached for a critical size, which has been estimated to be around 25 nm.[8,9] However, if the particle diameter exceeds a

[a] Dr. L. Altenschmidt, Dr. A. Bordage, Dr. E. Rivière, Dr. G. Fornasieri, Prof. A. Bleuzen
Institut de Chimie Moléculaire et des Matériaux d'Orsay
Université Paris-Saclay, CNRS 91400 Orsay (France)
E-mail: anne.bleuzen@universite-paris-saclay.fr

[b] Dr. P. Beaunier
Laboratoire de Réactivité de Surface, LRS
Sorbonne Université, CNRS
75005 Paris (France)

Supporting information for this article is available on the WWW under https://doi.org/10.1002/cnma.202200469

certain size, the coercive field decreases due to the transformation into the α-Fe_2O_3 phase. This transformation usually occurs when the diameter reaches 30 nm, but it can also reach 200 nm depending on the synthesis conditions.[16,20] Hence, to be able to design materials presenting an enhanced coercivity, the average particle size and the size distribution also have to be controlled.

So far, due to the specific synthetic conditions required to obtain the ε-Fe_2O_3 phase, materials containing this phase are generally obtained as nanostructures such as nanopowders, thin films[14,30–33] or nanowires.[34] And yet, for many applications, obtaining a large-size magnet is important. The synthesis of such large-size magnets, the magnetic properties of which arise from those of the ε-Fe_2O_3 phase, is very challenging since, starting from nano-powders, the ε-Fe_2O_3 nanoparticles are likely to grow and lose their properties during a densification step. Recently, bulk SiO_2/ε-Fe_2O_3 nanocomposites could be obtained following a four steps process,[27] that are 1) the preparation of an iron oxide polymer surrounded by a silica shell through a reverse micelle approach, 2) a calcination in air at 450–600 °C, 3) a fast current-activated pressure (100–300 MPa) assisted densification and 4) an annealing step at 1025 °C. Bulk magnets with Fe/Si ratio of 15 mol% and 90 mol% were thus obtained, exhibiting coercive fields of 15 and 12 kOe respectively.

In this work, we propose an alternative approach for the fabrication of ε-Fe_2O_3/SiO_2 nanocomposite bulk magnets based on the use of mesoporous ordered silica monoliths developed in our group.[35,36] The silica monolith is obtained by a sol-gel process, which opens the possibility to mold it into any desired macroscopic shape, which could besides be maintained during the thermal treatments (Scheme 1). The ordered mesoporosity allows for a homogeneous distribution of the iron oxide precursor in the silica matrix and the latter acts as an anti-sintering agent. Using the ordered and calibrated porosity allows the controlled synthesis of homogeneous nanoparticles with respect to their size and distribution due to a confined growth. At last, a fast reaction kinetics is imposed by a rapid increase of the temperature during the final thermal treatment. We determined the optimal synthesis conditions for the stabilization of the ε-Fe_2O_3 phase by varying the thermal treatment temperature and the Fe/Si ratio. The magnetic properties of the nanocomposites are thoroughly discussed in the context of the structural and morphological characteristics of the nanoparticles. The fine control of the iron oxide particle size and particle size distribution allowed us i) to precisely specify the size range of the ε-Fe_2O_3 particles with an enhanced coercivity and ii) to evidence a linear correlation between the coercivity and the mass percent of ε-Fe_2O_3 particles with this enhanced coercivity. This study allowed us to prepare, through a cheap and simple synthesis pathway, the ε-Fe_2O_3 based bulk magnet exhibiting the highest coercivity of 18 kOe.

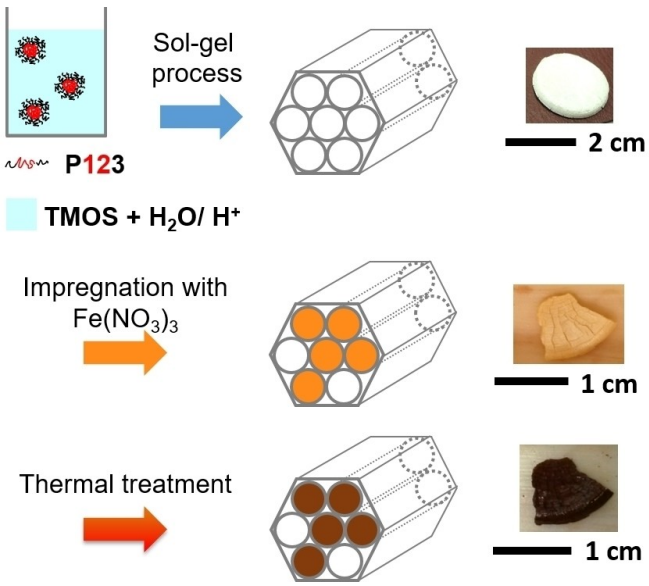

Scheme 1. Elaboration process of the ε-Fe_2O_3/SiO_2 monolith nanocomposite.

Results and Discussion

The monoliths were prepared by a simple procedure (Scheme 1) detailed in the experimental section consisting in three main steps. The first step is the formation by the sol-gel route in presence of a structure-directing agent of an ordered mesoporous silica monolith having a 2D hexagonal organization of the pores. Monoliths with very few cracks are obtained. The use of ordered mesoporous silica for the formation of the ε-Fe_2O_3 phase has already been reported,[37,38] but the compounds were obtained in the powder form, never in the form of a monolith, which is crucial to obtain a large-size magnet at the end of step 3. The second step is the impregnation of the ordered mesoporous silica monolith by a $Fe(NO_3)_3$ salt solution in order to introduce the precursor of the Fe_2O_3 phase in the porosity.[38–40] The third and last step is the thermal treatment, which transforms the precursors loaded in the porosity into the Fe_2O_3 phase and densifies the silica matrix. Upon the thermal treatments, the monolith breaks into few pieces, as shown on the photographs of Scheme 1. We did not try to determine conditions allowing for the formation of full crack-free monoliths since the monoliths have to be cut into small pieces for the magnetic measurements. Nevertheless, given the few cracks that form, the optimization of the aging conditions as well as of the heating and cooling rate of the thermal treatments should allow to get rid of them. The cracks mainly develop during the aging step that is to say during the drying of the gel. A better stiffening of the silica matrix combined with a slower evaporation of the solvent during this step is likely a key point towards crack-free blocks elaboration.

It is well established in the literature that the magnetic properties of Fe_2O_3 nanoparticles strongly depend on their synthesis conditions. In order to produce the block of silica containing ε-Fe_2O_3 particles with enhanced coercivity, we first varied the synthesis conditions of the Fe_2O_3 particles within the silica matrix and studied the effect of these synthesis conditions on the structure and morphology of the nanoparticles, and on the microstructure of the nanocomposites. Then, the magnetic

properties of the most relevant ground monoliths were studied in order to identify the optimal synthesis conditions and relate them to the structure and morphology of the Fe_2O_3 particles. At last, an enhanced coercivity at room temperature of magnets made of macroscopic pieces of monoliths could be evidenced.

A. Effect of the synthesis conditions on the structure and morphology of the nanocomposites

The Fe_2O_3 particles are formed by a thermal treatment in air with the fastest possible temperature ramp up to variable temperatures. The effect of two parameters on the structure and morphology of the nanocomposites were investigated: the final temperature of thermal treatment and the amount of iron nitrate salt loaded in the porosity of the matrix.

The diffraction patterns of **10%-700**, **10%-800**, **10%-900**, **10%-1000**, **10%-1100**, **10%-1200** and **10%-1300** are shown in Figure 1 (the nomenclature of the samples is given in the experimental section). All diffraction patterns exhibit the broad diffuse peak centered at 24°2θ arising from the amorphous silica matrix. In addition to this broad peak, the diffraction pattern of **10%-1300** also exhibits some peaks that can be assigned to cristobalite. All other peaks can be assigned to an iron oxide phase. It can be seen that, when the thermal treatment temperature is increased, the intensity of these diffraction peaks increases while the line width decreases. This can be attributed to an increase of the size of the diffraction domains and therefore to an increase of the crystallite size.

An identification of the formed iron oxide phase can be challenging since most of the lattice distances are very close from one phase to another. Nonetheless, it is possible to identify specific regions in the diffraction pattern with characteristic peaks for one polymorph, which enables to unambiguously assign the phase. For maghemite, it is the most intense (311) Bragg reflection at 35.6°2θ, for hematite the (012) diffraction line at 24.2°2θ, and for ε-Fe_2O_3 the double peak at 60.2°2θ and 60.9°2θ, corresponding to the (053) and (205) diffraction lines, respectively.[41] These regions are marked in blue in Figure 1.

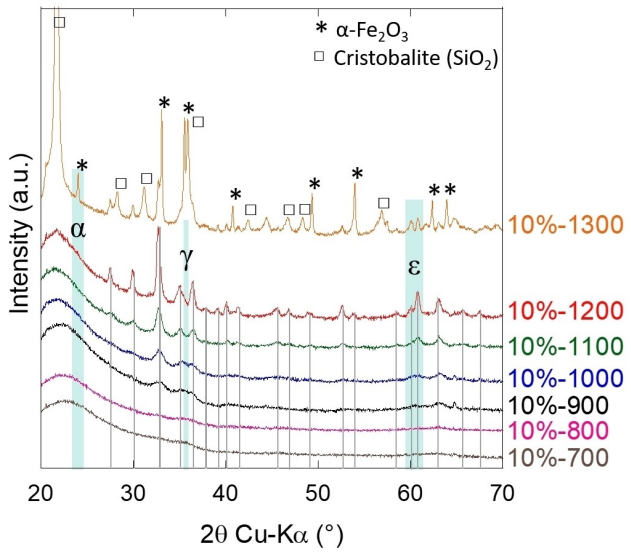

Figure 1. Powder X-ray diffraction patterns of **10%-700**, **10%-800**, **10%-900**, **10%-1000**, **10%-1100**, **10%-1200** and **10%-1300**. The regions marked in blue correspond to the region of the diffraction peaks typical for only the indicated Fe_2O_3 iron oxide phase. The grey lines represent the peaks, which can be indexed within the ε-Fe_2O_3 phase.

For thermal treatment temperatures below 900 °C, the diffraction peaks are strongly broadened and present a low intensity. The presence of diffraction peaks around the position of the (311) and (440) maghemite diffraction peaks suggests the presence of this iron oxide phase. This is also in agreement with other reports stating that the maghemite phase is formed as the first of the different Fe_2O_3 phases when the thermal treatment temperature is increased.[17]

It can be seen that with increasing the thermal treatment temperature, more reflections corresponding to the ε-Fe_2O_3 phase can be identified. The diffraction pattern of **10%-900** is the first to present the peaks that can be indexed within the ε-Fe_2O_3 phase. The diffraction patterns of **10%-1000**, **10%-1100** and **10%-1200** can also all be indexed in the ε-Fe_2O_3 phase. No diffraction peak corresponding to other crystallographic phases can be observed for these nanocomposites.

In contrast, the diffraction pattern of **10%-1300** is significantly different from the other ones. In addition to the diffraction lines of the ε-Fe_2O_3 phase, some diffraction peaks can be assigned to cristobalite as well as to the hematite (α-Fe_2O_3) phase. It seems that the crystallization of the silica matrix into cristobalite is accompanied by the formation of hematite, as it was also previously reported.[22,25]

Hence, powder XRD enables to conclude that, for our nanocomposites, a treatment temperature of at least 900 °C is required to induce the transformation of the maghemite phase into the ε-Fe_2O_3 one. For treatment temperatures below 900 °C, only the formation of maghemite is observed, while above 1300 °C the formation of hematite can be seen.

The TEM images of **10%-700** and **10%-800** are shown in Figure S1. The porosity of the hexagonally ordered silica matrix is clearly visible in both cases. The nanoparticles are aligned in a chain-like manner along the length of the pores. In **10%-700**, they present a diameter of 4.3 ± 0.7 nm and in **10%-800** the particles have a size of 5.3 ± 0.8 nm. The particles size distribution is particularly narrow and the average size is in good agreement with the diameter of the silica pores (5–6 nm as determined by N_2 physisorption[42]), indicating that the particles growth has been well confined within the porosity. The HR-TEM images (Figure S1c and S1f) show lattice planes spreading over the entire nanoparticle, indicating a monocrystalline character of the particles. However, it is not possible to clearly assign the distances to one of the iron oxide phases due to the similarities of the crystal structures and thereby the similar lattice plane distances.

Figure 2 shows the TEM analysis of **10%-900**, **10%-1000** and **10%-1100**. Regardless of the thermal treatment temperature, the ordered porosity with its parallel channels can still be seen. The nanoparticles all present a spherical shape and are

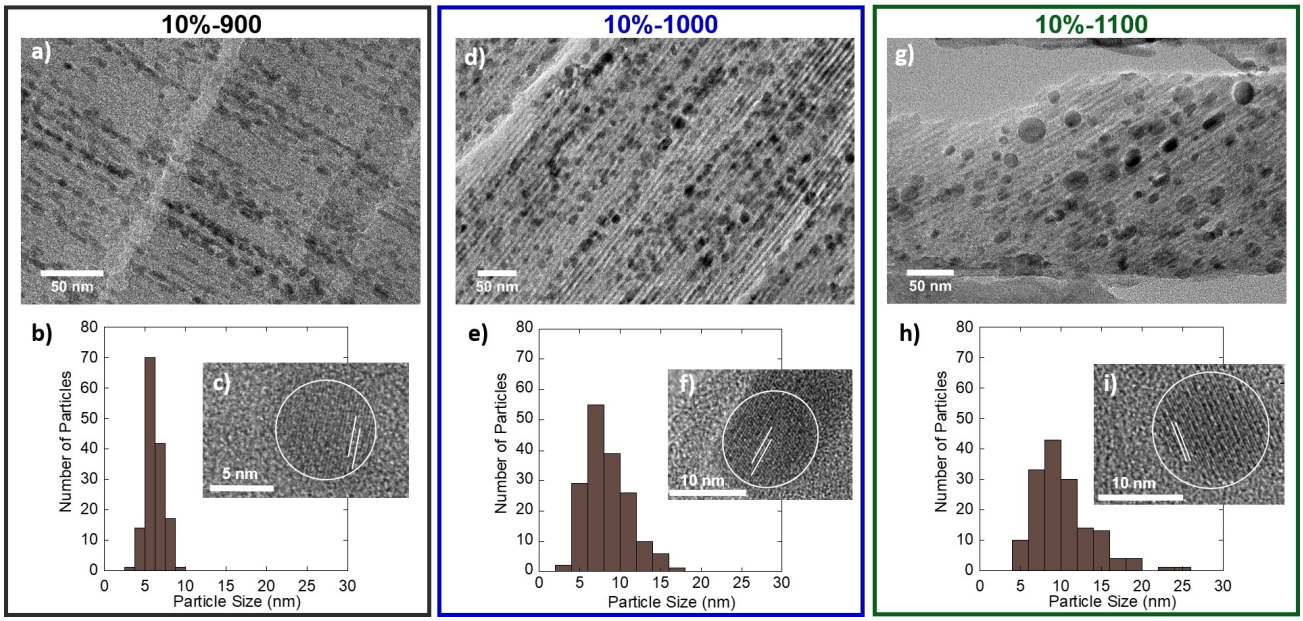

Figure 2. Representative TEM images, particle size distributions and HR-TEM images of **10%-900** (a, b and c), **10%-1000** (d, e and f), **10%-1100** (g, h and i).

embedded within the silica matrix. The particle size and distribution for the nanoparticles in **10%-900** is 6.2 ± 1.0 nm; this size is still close to the diameter of the silica pores, showing a good confinement effect of the surrounding matrix on the iron oxide particles' growth. However, for treatment temperatures above 1000 °C, the silica begins to soften, allowing the aggregation of iron oxide crystals.[17] This results in the increase of the particle size in **10%-1000** to 8.4 ± 2.6 nm and 10.3 ± 3.6 nm in **10%-1100**, and thus an expansion of the nanoparticles beyond the diameter of the silica pores.

Interestingly, not only the average particle size increases with the increase of the thermal treatment temperature but also the particle size distribution. The higher the temperature, the wider the distribution becomes. With the softening of the silica matrix at high temperatures, the particles are able to push into the silica walls and increase in size. Looking at the distribution of the particle sizes, it can be seen that despite the overall increase in particle size, some small particles remain. The HR-TEM images of **10%-900**, **10%-1000** and **10%-1100** (Figure 2c, f and i) reveal that the nanoparticles are monocrystalline regardless of their size. Due the absence of specific lattice planes, it is not possible to unambiguously assign the visible ones to a particular iron oxide phase.

For **10%-1200** the morphological characterization by TEM is presented in Figure 3. The first observation that can be made is that the silica matrix no longer presents its organized porosity. It appears that the silica matrix melted during the thermal treatment and the spherical nanoparticles are completely embedded in this densified matrix. From the HR-TEM image (Figure 3c), it can be seen that the nanoparticles are highly monocrystalline. Furthermore, we were able to unambiguously index all the lattice planes to the ε-Fe_2O_3 phase (Figure 3d). The average particle size for **10%-1200** is 16.5 ± 6.2 nm. With

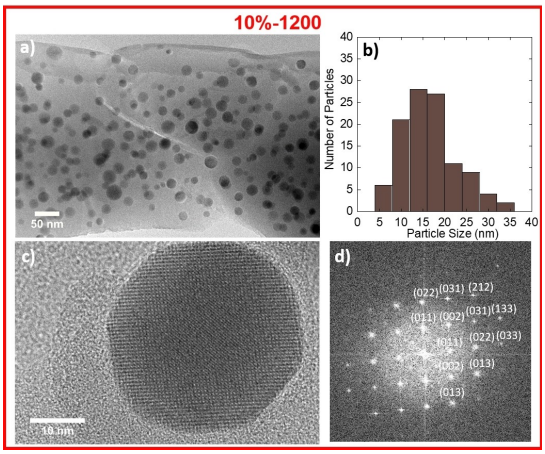

Figure 3. TEM characterization of **10%-1200**: a) Representative TEM image, b) particle size distribution, c) HR-TEM image and d) Fourier-transform of the HR-TEM image with indexation of the ε-Fe_2O_3 phase.

increasing thermal treatment temperature, the average particle size increases and the distribution becomes wider. This is a continuation and even an accentuation of the trend already seen for **10%-900**, **10%-1000** and **10%-1100** (Figure 2).

When the treatment temperature is increased to 1300 °C in **10%-1300** (Figure S2), the iron oxide nanoparticles are again embedded in the densified silica matrix, as it was the case for **10%-1200**. Moreover, in certain regions, the crystallization of cristobalite (Figure S2b) can be seen, as also evidenced by the diffraction peaks in Figure 1. The average particle size and the size distribution further increases to 28.4 ± 9.2 nm. As it was the case for the nanoparticles in the other nanocomposites, the formation of monocrystalline particles is also observed for **10%-1300** (Figure S2d).

From this TEM analysis, we can conclude that the average particle size and the size distribution progressively increase with increasing the temperature of the thermal treatment. The silica matrix is also modified as the thermal treatment temperature increases, and its evolution can be divided into three stages. First, the silica matrix retains its organized mesoporosity (**10%-700** and **10%-800**) and the iron oxide nanoparticles are confined in the pores. Then, a softening of the silica matrix (**10%-900**, **10%-1000** and **10%-1100**) is observed; the entering into this second stage is accompanied by an increase of both the average particle size and size distribution, and the formation of the ε-Fe_2O_3 phase is observed. In the third stage (**10%-1200** and **10%-1300**), a densification of the silica matrix occurs. The ε-Fe_2O_3 phase can be stabilized until the silica matrix begins to crystallize, which is accompanied by the formation of the hematite phase. Since in the first stage the formation of the ε-Fe_2O_3 phase could not be observed, we focused the further structural characterization on the nanocomposites obtained by a thermal treatment at 900 °C and above.

The TEM investigation shows the presence of residual small nanoparticles in the nanocomposites even at high treatment temperatures. Since the formation of the ε-Fe_2O_3 phase is size-dependent,[16] the presence of small nanoparticles could be related to the residual presence of the maghemite phase, which is not detected by XRD. The XRD study was therefore completed by a further investigation of the local order using Fe K-edge XANES (X-ray Absorption Near-Edge Structure) spectroscopy on the SAMBA beamline. The XANES spectra are presented in Figure 4a and a zoom of the pre-edge region in Figure 4b.

The white line of the hematite reference presents two distinct features at 7130.0 eV and 7134.0 eV, and the pre-edge also shows two peaks at 7113.5 and 7115.0 eV. The maghemite reference shows a broad white line maximum centered at 7133.0 eV, and a pre-edge peak centered at 7115.0 eV as well as a shoulder at low energy. These differences in the reference spectra can be assigned to the different local environments of the Fe^{3+} ions present in the Fe_2O_3 structure.[43,44]

It can be seen that the spectral feature of **10%-900**, **10%-1000**, **10%-1100** and **10%-1200** are similar. The white line maximum is located at 7133.0 eV and the pre-edge peak is broad and centered around 7114.5 eV. In contrast, the spectrum of **10%-1300** is clearly different from the other ones and resembles the one of the hematite reference, with the maximum at 7134.0 eV and a shoulder at 7130.0 eV in the white line. These XANES spectra confirm that the nanocomposites can be divided into two groups depending on the structure of their nanoparticles. In the first one, the nanoparticles consist mainly of the ε-Fe_2O_3 phase. **10%-900**, **10%-1000**, **10%-1100** and **10%-1200** belong to this first group. The strong similarity of the spectra to one another, different from those of maghemite and hematite, indicates that if those compounds contain an additional Fe_2O_3 phase, this phase is present in very low quantities. The second group contains the **10%-1300** nanocomposite, the spectrum of which presents the typical spectral features of the hematite phase. These observations are in agreement with the

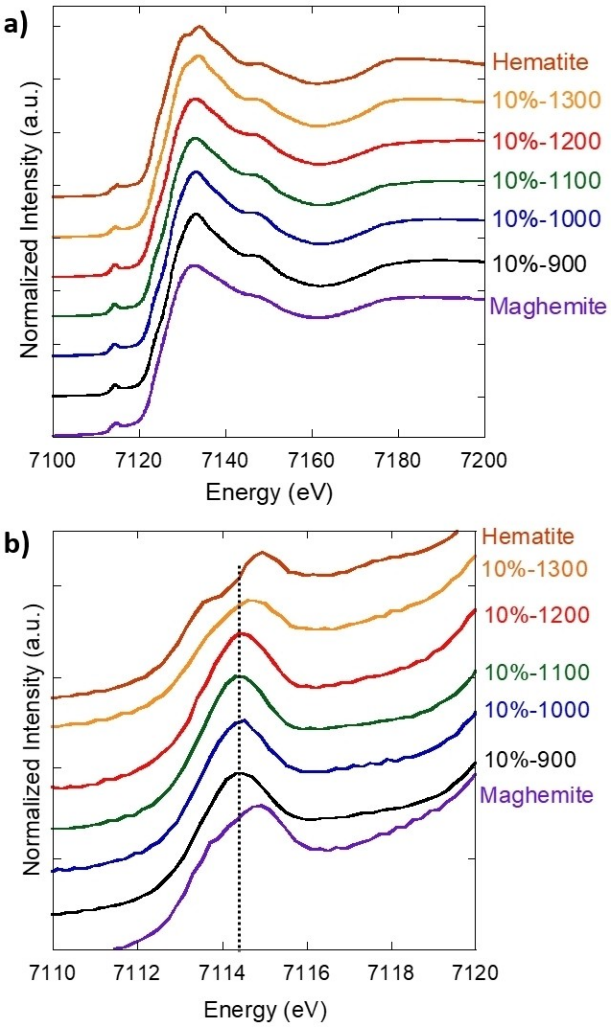

Figure 4. Normalized Fe K-edge X-ray absorption spectra of **10%-900**, **10%-1000**, **10%-1100**, **10%-1200** and **10%-1300** compared to the spectra of hematite and maghemite references.

results obtained by XRD (Figure 1), which show the transformation of one part of the ε-Fe_2O_3 phase into the hematite phase at 1300 °C.

The X-ray diffraction patterns of **5%-1100**, **10%-1100** and **20%-1100** are shown in Figure S3. All nanocomposites present the same diffraction peaks, which mainly differ in intensity. The diffraction lines are in agreement with the formation of the ε-Fe_2O_3 phase, suggesting that the Fe/Si ratio rather affects the particle size and/or the quantity of nanoparticles than the structure of the final phase. This is confirmed by the analysis of the XANES spectra of these three samples (Figure S4), which show very similar local structures around the Fe^{3+} ion in the three compounds.

The results of the TEM analysis of **5%-1100**, **10%-1100** and **20%-1100** are presented in Figure S5. It can be seen that the ordered parallel pore channels are still present regardless of the Fe/Si ratio. All the nanoparticles present a spherical shape and are embedded within the silica matrix. The particle sizes and their distributions (Figure S5b, d and f) are very close for the

three nanocomposites: 9.9 ± 2.7 nm for **5%-1100**, 10.3 ± 3.6 nm for **10%-1100**, and 11.9 ± 3.3 nm for **20%-1100**. From these results, it can be concluded that the evolution of the diffraction peaks is rather related to an increase of the quantity of Fe_2O_3 nanoparticles. Therefore, by varying the Fe/Si ratio, it is possible to maintain the average particle size of the nanoparticles (controlled by a confinement effect of the silica walls) and to change the overall quantity of nanoparticles present in the nanocomposite. This result opens interesting perspective for the preparation of materials with even higher Fe/Si ratio.

From the whole structural and morphological investigation of the nanocomposites by XRD, TEM and XAS, a relation between the average particle size, the Fe_2O_3 phase and the thermal treatment temperature can be established (Figure 5). Below 900 °C, the γ-Fe_2O_3 phase is formed. Between 900 °C and below 1300 °C, ε-Fe_2O_3 is obtained, while higher temperatures lead to the formation of α-Fe_2O_3. The particle size continuously increases from 700 °C up to 1100 °C, followed by a rupture of this trend and a steep increase of the particle size above treatment temperatures of 1100 °C. Therefore, our Fe_2O_3/SiO_2 nanocomposite system presents a particle size discontinuity at 1100 °C, suggesting significant changes in the properties of the nanocomposites at this temperature.

B. Magnetic properties of the ground ε-Fe_2O_3/SiO_2 nanocomposites

An enhanced coercivity being expected for particles made of the ε-Fe_2O_3 phase, the investigation of the magnetic properties focuses on the nanocomposites mainly containing those particles (i.e. the nanocomposites obtained by a thermal treatment at or above 900 °C). In a first step, the monoliths were ground for the magnetic measurements. This allowed us i) to get quantitative magnetic data, ii) to be sure that the analyzed fraction of monolith is representative of the whole material, and iii) to directly compare our results to the literature dealing with magnetic properties of powdered compounds.

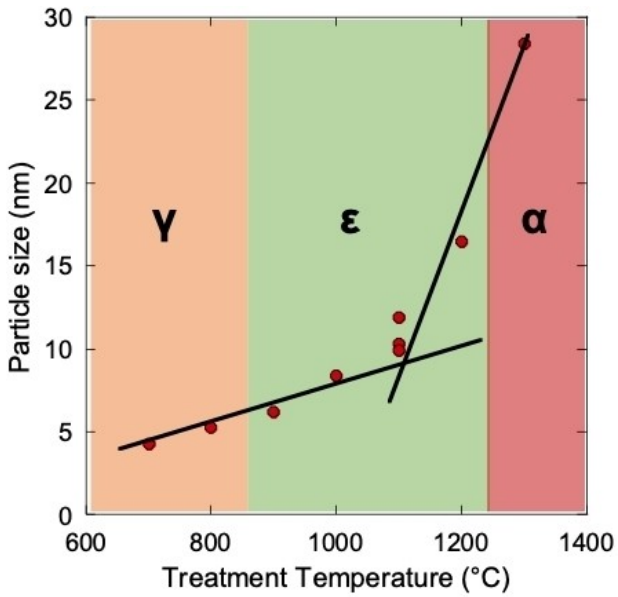

Figure 5. Representation of the dependence of the particle size determined by TEM with the treatment temperature. The black lines are a guide for the eyes. The temperature ranges in which the γ-, ε- and α- Fe_2O_3 phases are majorly present, as suggested by the XRD analysis, are represented by different colored backgrounds.

The ZFC-FC magnetization curves of **10%-900**, **10%-1000**, **10%-1100**, **10%-1200** and **10%-1300** are presented in Figure 6a–e. The shape of the magnetization curves depends on the thermal treatment temperature. The ZFC-FC magnetization curves of **10%-900** (Figure 6a) exhibits the characteristic profile for an assembly of superparamagnetic nanoparticles with a ZFC maximum assignable to the blocking/freezing temperature,[43] whereas those of **10%-1200** (Figure 6d) exhibits the typical magnetic transition of the ε-Fe_2O_3 phase between 150 K and 80 K.[46,47] The ZFC-FC magnetization curves of the nanocomposites resulting from thermal treatment temperatures between 900 °C and 1200 °C are intermediate between those of **10%-900** and **10%-1200**. With increasing the thermal treatment temperature, the magnitude of the magnetization change upon the magnetic transition increases. Meanwhile, the temperature of the ZFC maximum below 50 K varies, taking the value of 49 K in **10%-900**, 44 K in **10%-1000** and 28 K in **10%-1100**. These features can reflect the presence of two kinds of ε-Fe_2O_3 particles defined by their size in the nanocomposites. The first one corresponds to ε-Fe_2O_3 particles of size less than the critical threshold of 7.5 nm,[9] which exhibit a superparamagnetic behavior associated with a maximum of the ZFC magnetization curve in the low temperature range. The second one consists of the ε-Fe_2O_3 particles with a size above the critical one and expected to be ferrimagnetic at 300 K, with the characteristic magnetic transition between 150 and 80 K. A variation in the quantity of the ε-Fe_2O_3 particles belonging to each group (superparamagnetic or ferrimagnetic) can explain the evolution of the profile of the ZFC-FC magnetization curves from **10%-900** to **10%-1200** in the series of nanocomposites.

The evolution of the profile of the ZFC-FC magnetization curves shows a discontinuity between **10%-1200** and **10%-1300**. The strong decrease in the magnetization value at 300 K and in the magnitude of magnetization change upon the magnetic transition is in agreement with the presence of a significant amount of the α-Fe_2O_3 phase to the detriment of the ε-Fe_2O_3 phase in the latter nanocomposite, as shown by XRD and XAS data.

The ZFC-FC magnetization curves of **5%-1100**, **10%-1100** and **20%-1100** are presented in Figure 6f. All curves present the same shape regardless of the Fe/Si ratio. The main difference is the value of the magnetization, which increases as the Fe/Si ratio increases. The comparable shape of the curves can be explained by the comparable particle size distribution in the three nanocomposites (Figure 5) and the increasing magnetization values along the series by the increasing amount of ε-Fe_2O_3 particles formed in the monoliths as the amount of the $Fe(NO_3)_3$ precursor introduced in the silica matrix increases.

The magnetic field dependence of the magnetization measured at 300 K is shown in Figure 7 for **10%-900**, **10%-**

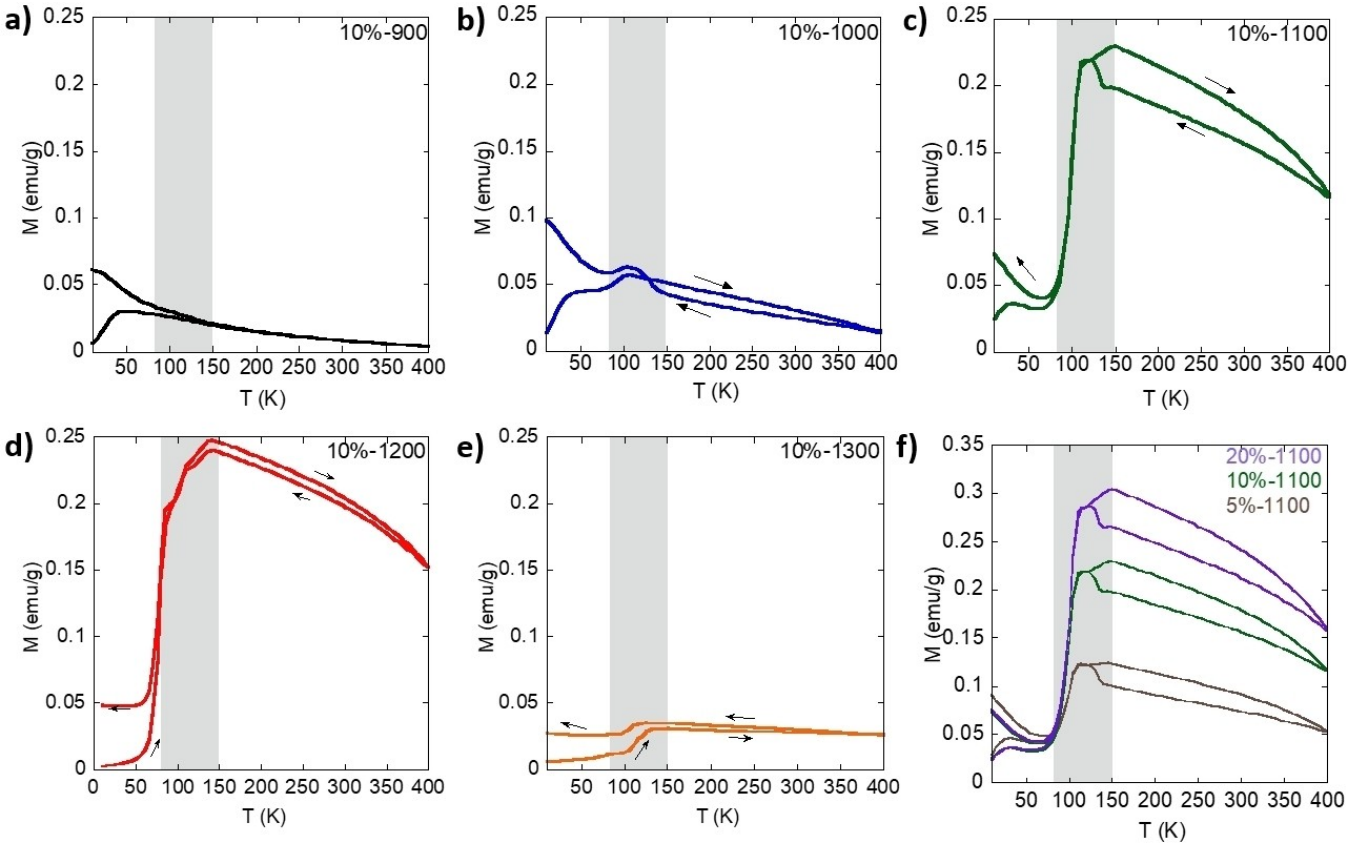

Figure 6. ZFC-FC magnetization curves of a) **10%-900**, b) **10%-1000**, c) **10%-1100**, d) **10%-1200** and e) **10%-1300**; f) Comparison of the ZFC-FC magnetization curves of **5%-1100**, **10%-1100** and **20%-1100**. The grey zone marks the temperature zone of the magnetic transition of the ε-Fe_2O_3 phase.

1000, **10%-1100**, **10%-1200** and **10%-1300**, and for **5%-1100**, **10%-1100** and **20%-1100**. In the **10%-T** series, the coercive field of the nanocomposite (H_C(NC)) continuously increases from H_C(NC) = 0 Oe (**10%-900**) to 500 Oe (**10%-1000**) to 6750 Oe (**10%-1100**) and finally to 17600 Oe (**10%-1200**). But, for **10%-1300**, H_C(NC) drops to 7100 Oe. The null coercive field of **10%-900** confirms the superparamagnetic character of the nanoparticles in this compound. The increasing value of H_C(NC) from **10%-900** to **10%-1200** is explained by the increasing average particle size of the ε-Fe_2O_3 phase (Figure 2 and 3).[9] The discontinuity in the variation of the coercive field between **10%-1200** (17600 Oe) and **10%-1300** (7100 Oe) is not surprising since the largest ε-Fe_2O_3 particles are transformed into hematite ones at 1300 °C.

With increasing the Fe/Si ratio (Figure 7f), the coercive field and the magnetization at 50 kOe increase. This is explained by the increasing average size and amount of ε-Fe_2O_3 particles respectively in the nanocomposites.

Plotting the coercive field of all studied nanocomposites against the average particle size determined by TEM (Figure S6) reveals that the coercive field starts to increase for particle sizes in the range of 6–8 nm. This is the same temperature range than the one determined by Ohkoshi *et al.*[9] and was set to be the superparamagnetic particle size limit (7.5 nm) of the ε-Fe_2O_3 particles. Moreover, the profile of the curve of coercivity against average particle size is similar to the one reported in their study. This result also shows that the coercive field depends on the average particle size rather than on their amount in the nanocomposite, which is expected for uncoupled magnetic particles.

Interestingly, most of the hysteresis loops of the nanocomposites exhibit a necking of the curve at H = 0 Oe. Such a complex shape of the hysteresis loop has already been assigned to the presence of several magnetic phases in the literature and, when these magnetic phases are not coupled, the dM/dH derivative curve displays well-defined peaks, the maximum of which corresponds to the coercive fields of the different magnetic phases.[48,49] We propose to assign these necking of the M(H) curves to the presence of a fraction of superparamagnetic ε-Fe_2O_3 or α-Fe_2O_3 nanoparticles in addition to a ferrimagnetic fraction, which is consistent with the ZFC/FC magnetization curves (Figure 6). The presence of two fractions of particles with well-defined coercive fields in the nanocomposites is confirmed by the derivatives of the magnetization with respect to the magnetic field (dM/dH) displayed in Figure S7. Three well-defined peaks can be observed on the dM/dH curves of most of the nanocomposites. The maximum at H = 0 Oe corresponds to a first fraction of nanoparticles with a superparamagnetic behavior, while the two symmetric maxima (centered here around H = ±17600 Oe) can be assigned to a

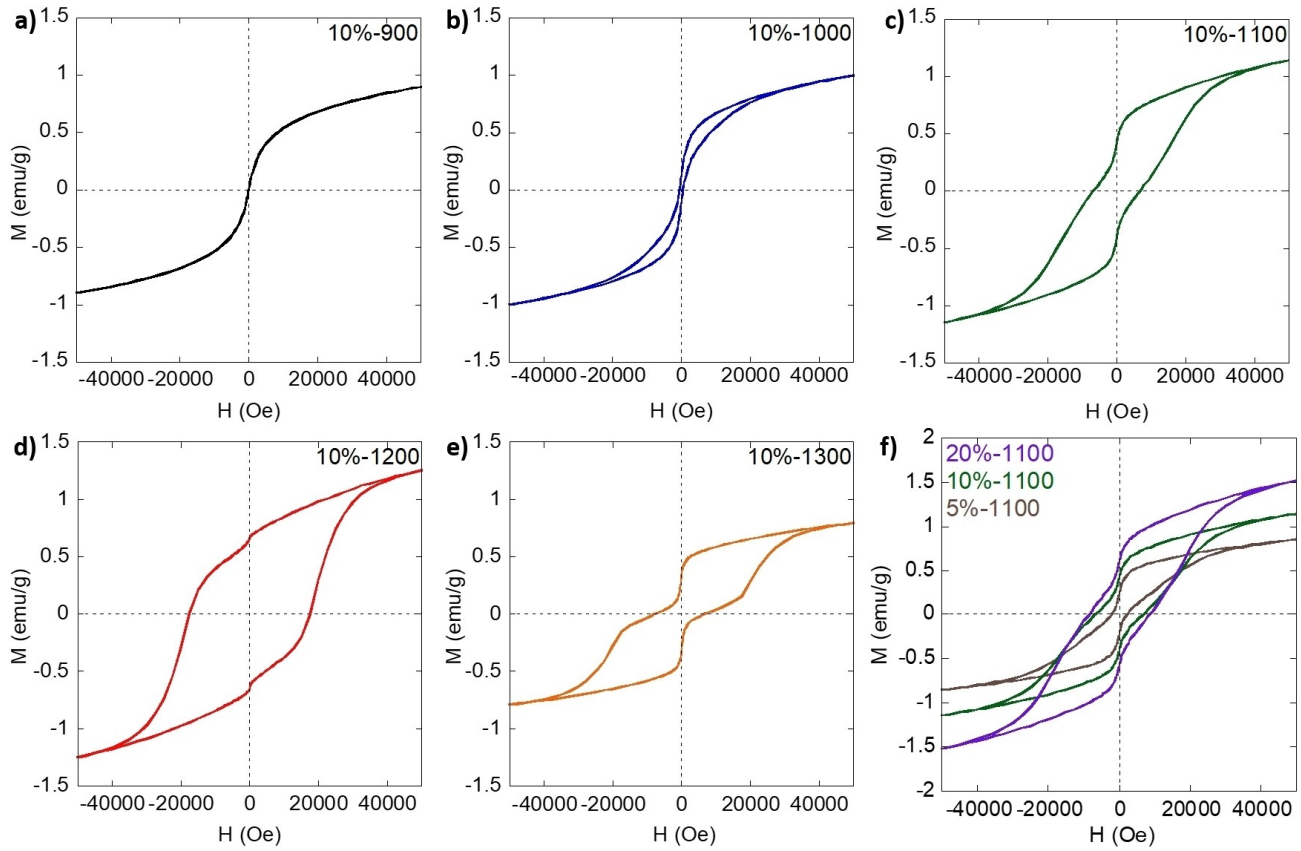

Figure 7. Magnetic field dependence of the magnetization measured at 300 K for a) **10%-900**, b) **10%-1000**, c) **10%-1100**, d) **10%-1200** and e) **10%-1300**; f) Comparison of the magnetic field dependence of the magnetization measured at 300 K of **5%-1100**, **10%-1100** and **20%-1100**.

second fraction of nanoparticles with a ferrimagnetic behavior and H_C(NP) = 17600 Oe. In the following, we define H_C(NP) as the coercive field of the nanoparticles contained in the nanocomposite to distinguish it from the coercive field of the nanocomposite (H_C(NC)). These peaks can be assigned to the reorientation of the magnetization for a population of ε-Fe_2O_3 nanoparticles with H_C(NP) = 0 Oe and H_C(NP) = 17600 Oe. Thus, the shape of the M(H) and the dM/dH curves indicates that most of the nanocomposites contain both fractions of nanoparticles and that their magnetic properties depend on the amount of the different fractions. The higher the fraction of nanoparticles with H_C(NP) = 17600 Oe, the higher the coercive field of the nanocomposite (H_C(NC)). The previous sections show that the nanoparticles contained in the nanocomposites of the magnetic study are essentially made of the ε-Fe_2O_3 phase, except for **10%-1300**, which also contains a significant amount of the α-Fe_2O_3 phase. The nanoparticles with a coercive field H_C(NP) = 17600 Oe are those made of the ε-Fe_2O_3 phase having a size above a critical threshold, the value of which remains to be determined.

In order to test the hypothesis formulated above that the magnetic coercivity depends on the percentage of nanoparticles with H_C(NP) = 17600 Oe in the nanocomposite, we have tried to correlate it with the mass percent of the corresponding nanoparticles. The magnetic coercivity of the nanocomposites is characterized by the coercive field H_C(NC), which seems to vary as the intensity of dM/dH at 17600 Oe (dM/dH_{17600}). H_C(NC) and (dM/dH_{17600}) are given in Table S1 for **10%-1000**, **10%-1100**, **10%-1200**, **10%-1300**, **5%-1100** and **20%-1100**. From the particle size distribution histograms (Figure 2 and 3), i.e. the number of particles corresponding to each diameter, one can evaluate the total volume of particles and then the mass percentage (mass%) of particles corresponding to each diameter. These data are gathered in Tables S2 to S8.

The M(H) and dM/dH curves of **10%-900** show that the H_C(NC) and dM/dH_{17600} values are equal to zero, and yet Table S2 shows that a small mass percentage of nanoparticles have a size above the critical superparamagnetic grain size (7.5 nm). This suggests that their quantity and/or size are not high enough to have a detectable impact on the coercivity of the nanocomposite.

In contrast, the M(H) and dM/dH curves of **10%-1200** show that this nanocomposite exhibits the highest H_C(NC) and dM/dH_{17600} values. This nanocomposite therefore contains the highest amount of nanoparticles with H_C(NP) = 17600 Oe. Furthermore, the very small step at 0 Oe on the M(H) curve shows that this nanocomposite only contains a very small mass percentage of nanoparticles with H_C(NP) = 0. Table S5 and the previous sections show that this nanocomposite essentially contains ε-Fe_2O_3 nanoparticles and that the size of 97% of them

is comprised between 14 and 34 nm. Taking these values as the two low and high diameter thresholds for the ε-Fe_2O_3 nanoparticles with H_C(NP) = 17600 Oe, one can determine for each nanocomposite the mass percentage of nanoparticles having sizes comprised between these two values (Table S9). The plot of H_C(NC) as a function of this mass percentage (Figure 8) shows a linear correlation, meaning that the magnetic coercivity indeed depends on the mass percentage of nanoparticles with diameter comprised between 14 and 34 nm. dM/dH_{17600} shows the same linear dependence with this mass percent (Figure S8b), which also suggests a linear correlation between H_C(NC) and dM/dH_{17600} (Figure S8a). These results show that the coercive field of the nanocomposites is directly linked to the mass percent of nanoparticles with H_C(NP) = 17600 Oe. The fact that the variation of H_C(NC) and dM/dH_{17600} with the mass percentage of nanoparticles progressively departs from linearity as the low or high size threshold is increased or decreased (Figure S9) confirms the particles size range with H_C(NP) = 17600 Oe from 14 to 34 nm in our nanocomposites. Thus, this study allows us to specify the characteristics of the ε-Fe_2O_3 nanoparticles with enhanced coercivity.

In summary, the analysis above shows that in our nanocomposites the nanoparticles originating the enhanced magnetic coercivity are those with a size ranging from 14 to 34 nm (H_C(NC) = 17600 Oe) and the magnetic coercivity of the nanocomposite is directly linked to the mass percentage of these nanoparticles in the assembly. 14 nm corresponds to the diameter above which the ε-Fe_2O_3 particles are ferrimagnetic with the enhanced coercive field characteristic of the ε-Fe_2O_3 phase. This size threshold should be inherent to the ε-Fe_2O_3 phase. 34 nm is the size at which the ε-Fe_2O_3 to α-Fe_2O_3 transformation occurs in our synthesis conditions. This threshold depends on kinetic and thermodynamic parameters and therefore on the synthesis conditions.

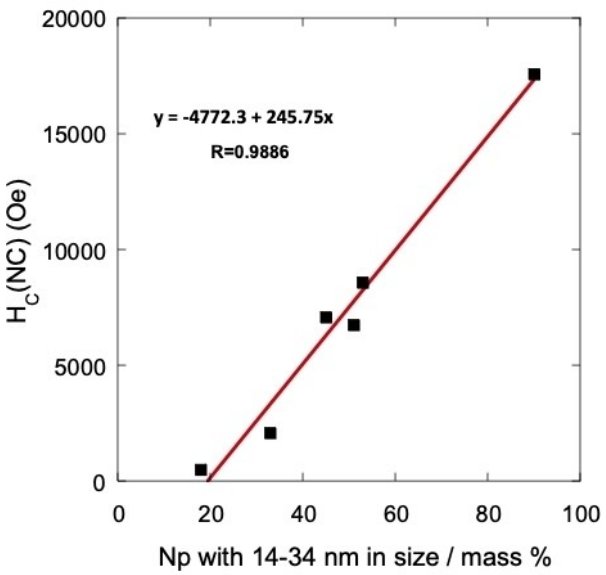

Figure 8. H_C(NC) as a function of the mass percent of nanoparticles having sizes comprised between 14 and 34 nm.

C. Macroscopic pieces of monoliths with enhanced coercivity

One of the advantages of using the sol-gel route for the preparation of the ordered mesoporous silica monoliths is that a macroscopic material with well-defined shape can be directly obtained by molding, without any additional processing step.

The structural, morphological and magnetic characterization of the grinded nanocomposites revealed that the quantity of ε-Fe_2O_3 nanoparticles originating the desired enhanced coercivity, increases with the thermal treatment temperature. **10%-1100** and **10%-1200** were therefore chosen for the magnetic study of a macroscopic piece of monolith due to their large content of the desired ε-Fe_2O_3 nanoparticles.

Interestingly, the pieces of monoliths are attracted to a NdBFe magnet at room temperature, as shown in the insets of Figure 9.

The magnetic field dependences of the magnetization of a piece of monolith (4 $mm^2 \times 1$ mm) of **10%-1100** and **10%-1200** are shown in Figure 9. The coercive field (H_C(NC)) of **10%-1100** and **10%-1200** are 7750 Oe and 18170 Oe respectively. These values are in the same range as the ones of the ground nanocomposites (Figure 7). The differences can be assigned to small variations from one synthesis to the other.

Interestingly, the field-dependent magnetization curves of an anisotropic piece of monolith with an elongated bar shape (3.6 mm × 1.1 mm) measured with the long axis placed parallel or perpendicular to the applied magnetic field superimpose (Figure S10), showing the random crystallographic orientation of ε-Fe_2O_3 particles in the monoliths also confirmed by electron diffraction (Figure S11). Thus, the magnetic properties of the material do depend neither on its shape nor on its orientation.

This hence demonstrates that, following our approach, it is possible to prepare a ε-Fe_2O_3 based bulk magnet with enhanced coercivity at room temperature.

Conclusion

We presented an efficient alternative route for the fabrication of ε-Fe_2O_3 based bulk magnet with enhanced coercivity at room temperature. In comparison with the previously reported approach,[27] our compounds contain a lower amount of the ε-Fe_2O_3 phase. A rough estimation of the volume % of ε-Fe_2O_3 in the nanocomposites can be done by considering a dense silica matrix. The volume % ranges from 3.5 to 15% and the mol % from 2.5 to 10%, which is significantly lower than those in the previous work (mol % ranging from 15 to 90%). A multi-step impregnation would allow significantly raising the ε-Fe_2O_3 phase content in our case. If we now compare the coercive field of the material, for comparable ε-Fe_2O_3 phase content, it is higher in our material (up to 18179 Oe against 15000 Oe).

Our approach offers a fine control of the size and size distribution of the ε-Fe_2O_3 nanoparticles. We could thus first establish that the magnetic coercivity is linearly correlated to the mass percent of the particles with an enhanced coercivity in the nanocomposites. We were then able to specify the characteristics of the particles with enhanced coercivity, which

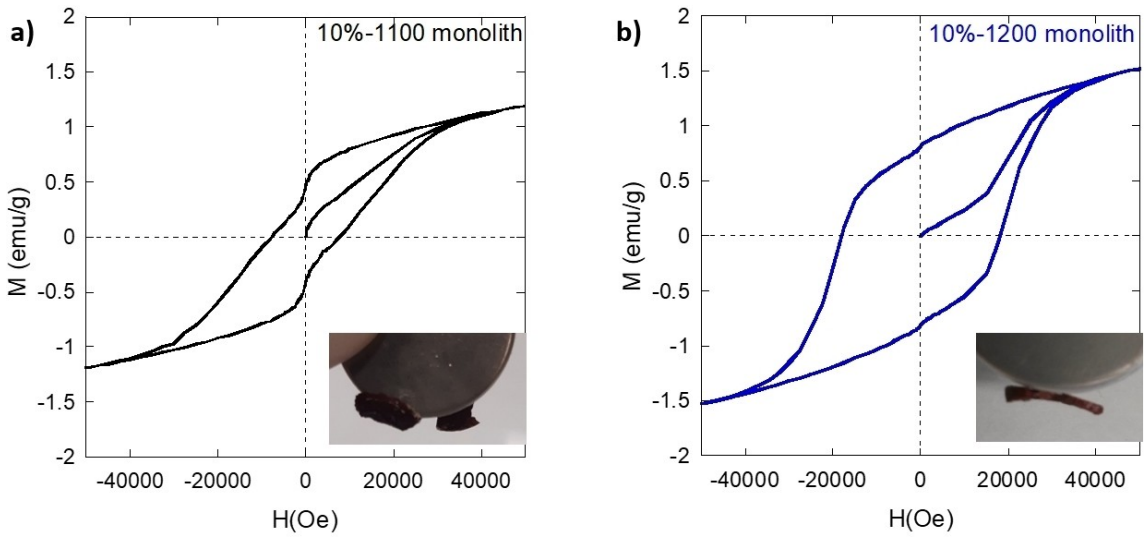

Figure 9. Magnetic field dependence of the magnetization measured at 300 K of a) **10%-1100** and b)**10%-1200** in their monolithic form. Insets: Photos showing the magnetic attraction to a NdFeB magnet of the thermally treated monolith at room temperature.

are made of the ε-Fe_2O_3 phase with a diameter above 14 nm. Furthermore, the versatility of the fabrication process opens up new perspectives towards the fabrication of crack-free molded blocks, with increased Fe/Si ratio or with substituted ε-$M_xFe_{2-x}O_3$ nanoparticles. Taking advantage of the processing flexibility inherent in the sol-gel route used for the synthesis of the hexagonally ordered silica monolith, the optimization of the fabrication process should allow for the molding of the entire monolith into any desired shape. At last, this work highlights the interest to start from ε-Fe_2O_3-loaded mesoporous silica for the preparation of rare-earth-free materials with high coercivity, opening new perspectives in terms of synthetic strategies combining different approaches such as ε-Fe_2O_3 ALD (Atomic Layer deposition) in mesoporous silica membranes for instance.

Experimental Section

A. Syntheses

The synthesis of the hexagonal ordered mesoporous silica monolith is described elsewhere in detail.[35] For a typical synthesis, 2.6 g of the P123 co-polymer were dissolved in 4 g tetramethyl orthosilicate (TMOS). 2 mL of distilled water (pH = 1.4, adjusted with HNO_3) were added under stirring and the formed sol was left ageing in a closed vial for 1 hour at 23 °C. The gel was aged for 1 week at 23 °C in air and finally calcined at 500 °C in air.

For the preparation of the nanocomposites (silica monolith + nanoparticles inside), the silica monolith was impregnated with different Fe/Si molar ratios using $Fe(NO_3)_3 \cdot 9\ H_2O$. The impregnation solutions for the ε-Fe_2O_3 samples were prepared with a Fe/Si ratio of 5, 10 and 20 mol%, corresponding to 600 mg, 1200 mg and 2400 mg of $Fe(NO_3)_3 \cdot 9\ H_2O$, respectively, dissolved in 1 mL of distilled water. For the loading of the pores with the iron solution, the silica monolith was immersed in heptane and a volume of the impregnation solution corresponding to 80% (0.56 mL for 1 g of SiO_2) of the porous volume was added. After approximately 15 minutes, the heptane was removed and the monoliths dried in air overnight.

To study the effect of the treatment temperature, the dried nanocomposites with a Fe/Si ratio of 10 mol% were thermally treated up to a final temperature ranging from 700 °C to 1300 °C. During this thermal treatment, the oven temperature was increased as rapidly as possible and, upon reaching the target temperature, was left cooling down to room temperature immediately. Two muffle furnaces were used for the thermal treatments depending on the targeted temperature: the Nabertherm model L 3/11/P320 for thermal treatments up to 1100 °C and the Nabertherm model LHT 04/17 for thermal treatment above 1100 °C. The needed times to reach the targeted temperatures are as follows: 27 min for 700 °C, 34 min for 800 °C, 44 min for 900 °C, 57 min for 1000 °C, 72 min for 1100 °C, 16 min for 1200 °C and 22 min for 1300 °C. In all cases, it took 8 h to cool the samples to room temperature. The samples are denoted **10%-T**, where **T** corresponds to the used thermal treatment temperature (in °C).

For the second series, the effect of the Fe/Si ratio was analyzed. The nanocomposites with a Fe/Si ratio of 5, 10 and 20 mol% were thermally treated at 1100 °C. The samples are denoted **Y%-1100**, where **Y** corresponds to the initial Fe/Si ratio.

The maghemite and hematite references were prepared as bulk powders. The maghemite sample was prepared following the protocol of Cao *et al.*[50] using a temperature of 150 °C. The hematite reference was obtained by thermally treating $Fe(NO_3)_3 \cdot 9\ H_2O$ at 1000 °C using the same thermal treatment as for the nanocomposites.

B. Characterizations

The nanocomposites were analyzed after being finely ground.

The powder X-ray diffraction analysis was performed on a Philips X'Pert diffractometer equipped with a Cu-K_α cathode ($\lambda = 1.54$ Å). The acquisition was performed during 12 hours with a step size of 0.033° 2θ using an Al sample holder.

The transmission electron microscope images were collected on a JEOL JEM 2010 UHR and a JEOL JEM 2100 Plus microscopes (LaB_6

filament and operating at 200 kV) equipped with a CCD camera (Gatan Orius Sc 1000). The particle sizes were determined using the ImageJ software and the value of the standard deviation is given.

The Fe K-edge X-ray absorption spectroscopy (XAS) experiments were performed on the SAMBA beamline (SOLEIL, Gif-sur-Yvette, France).[51] The samples were placed between two pieces of kapton tape on a punched cardboard. The spectra were recorded at room temperature in the transmission mode from 6900 eV to 8300 eV using the continuous mode of the monochromator. No radiation damage was observed during the acquisition. All spectra were normalized and energy-calibrated using the Athena software after measurements.[52]

Magnetic properties were investigated using a Quantum Design MPMS-5S and a Quantum Design XL-7 SQUID magnetometers. The zero-field-cooled (ZFC) and field-cooled (FC) magnetization curves were measured between 5 and 400 K with an applied magnetic field of 50 Oe. The magnetic field dependence of magnetization was recorded at 300 K for a magnetic field varying between −50000 Oe (−5 T) and 50000 Oe (5 T). The magnetization value is given as emu per gram of nanocomposite.

The XRD, SEM, and magnetic measurements were done at the instrumentation platform of the Institut de Chimie Moléculaire et des Matériaux d'Orsay (ICMMO) at Université Paris-Saclay. The TEM analysis was done at the technical platform of the Institut des Matériaux de Paris Centre (IMPC) at Sorbonne Université.

Acknowledgements

This research was supported by Paris-Saclay University and the CNRS. The authors acknowledge SOLEIL for provision of synchrotron radiation facilities on the SAMBA beamline through proposal 20180973. The authors thank G. Landrot (SAMBA beamline, SOLEIL) for help during the experiments. L.A. thanks the French government for the PhD financial support.

Conflict of Interest

The authors declare no conflict of interest.

Data Availability Statement

The data that support the findings of this study are available on request from the corresponding author. The data are not publicly available due to privacy or ethical restrictions.

Keywords: Hard magnet · Ordered mesoporous silica monolith · ε-Fe_2O_3

[1] R. C. Pullar, *Prog. Mater. Sci.* **2012**, *57*, 1191–1334.
[2] N. Jones, *Nature* **2011**, *472*, 22–23.
[3] A. D. Volodchenkov, Y. Kodera, J. E. Garay, *J. Mater. Chem. C* **2016**, *4*, 5593–5601.
[4] K. Inomata, T. Sawa, S. Hashimoto, *J. Appl. Phys.* **1988**, *64*, 2537–2540.
[5] S. H. Sun, C. B. Murray, D. Weller, L. Folks, A. Moser, *Science* **2000**, *287*, 1989–1992.
[6] J. Jin, S.-I. Ohkoshi, K. Hashimoto, *Adv. Mater.* **2004**, *16*, 48–51.
[7] A. Namai, M. Yoshikiyo, K. Yamada, S. Sakurai, T. Goto, T. Yoshida, T. Miyazaki, M. Nakajima, T. Suemoto, H. Tokoro, S.-I. Ohkoshi, *Nat. Commun.* **2012**, *3*, 1035.
[8] M. Popovici, M. Gich, D. Niznansky, A. Roig, C. Savii, L. Casas, E. Molins, K. Zaveta, C. Enanche, J. Sort, S. de Brion, G. Chouteau, J. Nogués, *Chem. Mater.* **2004**, *16*, 5542–5548.
[9] S.-I. Ohkoshi, A. Namai, K. Imoto, M. Yoshikiyo, W. Tarora, K. Nakagawa, M. Komine, Y. Miyamoto, T. Nasu, S. Oka, H. Tokoro, *Sci. Rep.* **2015**, *5*, 14414.
[10] E. Gorbachev, M. Soshnikov, M. Wu, L. Alyabyeva, D. Myakishev, E. Kozlyakova, V. Lebedev, E. Anokhin, B. Gorshunov, O. Brylev, P. Kazin, L. Trusov, *J. Mater. Chem. C* **2021**, *9*, 6173–6179.
[11] M. Kurmoo, J. Rehspringer, A. Hutlova, C. D'Orleans, S. Vilminot, C. Estournes, D. Niznansky, *Chem. Mater.* **2005**, *17*, 1106–1114.
[12] S.-I. Ohkoshi, S. Kuroki, S. Sakurai, K. Matsumoto, K. Sato, S. Sasaki, *Angew. Chem. Int. Ed.* **2007**, *46*, 8392–8395; *Angew. Chem.* **2007**, *119*, 8544–8547.
[13] A. Namai, S. Sakurai, M. Nakajima, T. Suemoto, K. Matsumoto, M. Goto, S. Sasaki, S.-I. Ohkoshi, *J. Am. Chem. Soc.* **2009**, *131*, 1170–1173.
[14] S.-I. Ohkoshi, K. Imoto, A. Namai, S. Anan, M. Yoshikiyo, H. Tokoro, *J. Am. Chem. Soc.* **2017**, *139*, 13268–13271.
[15] M. Gich, I. Fina, A. Morelli, F. Sanchez, M. Alexe, J. Gazquez, J. Fontcuberta, A. Roig, *Adv. Mater.* **2014**, *26*, 4645–4652.
[16] S. Lee, H. Xu, *J. Phys. Chem. C* **2016**, *120*, 13316–13322.
[17] S. Sakurai, A. Namai, K. Hashimoto, S.-I. Ohkoshi, *J. Am. Chem. Soc.* **2009**, *131*, 18299–18303.
[18] V. N. Nikolić, M. Tadić, M. Panjan, L. Kopanja, N. Cvjetićanin, V. Spasojević, *Ceram. Int.* **2017**, *43*, 3147–3155.
[19] S.-I. Ohkoshi, S. Sakurai, J. Jin, K. Hashimoto, *J. Appl. Phys.* **2005**, *97*, 10K312.
[20] J. Tuček, R. Zbořil, A. Namai, S.-I. Ohkoshi, *Chem. Mater.* **2010**, *22*, 6483–6505.
[21] A. Navrotsky, L. Mazeina, J. Majzlan, *Science* **2008**, *319*, 1635–1638.
[22] E. Tronc, C. Chanéac, J. P. Jolivet, *J. Solid State Chem.* **1998**, *139*, 93–104.
[23] G. A. Bukhtiyarova, M. A. Shuvaeva, O. A. Bayukov, S. S. Yakushkin, O. N. Martyanov, *J. Nanopart. Res.* **2011**, *13*, 5527–5534.
[24] R. Zboril, M. Mashlan, K. Barcova, M. Vujtek, *Hyperfine Interact.* **2002**, *139/140*, 597–606.
[25] E. Taboada, M. Gich, A. Roig, *ACS Nano* **2009**, *3*, 3377–3382.
[26] J. Lopez-Sanchez, A. Munoz-Noval, A. Serrano, M. Abuín, J. de la Figuera, J. F. Marco, L. Perez, N. Carmona, O. Rodríguez de la Fuente, *RSC Adv.* **2016**, *6*, 46380–46387.
[27] K. T. Chan, J. R. Morales, Y. Kodera, J. E. Garay, *J. Mater. Chem. C* **2017**, *5*, 7911–7918.
[28] V. N. Nikolic, V. Spasojevic, M. Panjan, L. Kopanja, A. Mrakovic, M. Tadic, *Ceram. Int.* **2017**, *43*, 7497–7507.
[29] J. Cleron, A. A. Baker, T. Nakotte, A. Troksa, J. Han, *J. Phys. Chem. C* **2022**, *126*, 7256–7263.
[30] T. Amrillah, L. T. Quynh, C. Nguyen Van, T. H. Do, E. Arenholz, J. Y. Juang, Y. H. Chu, *ACS Appl. Mater. Interfaces* **2021**, *13*, 17006–17012.
[31] M. Gich, J. Gazquez, A. Roig, A. Crespi, J. Fontcuberta, J. C. Idrobo, S. J. Pennycook, M. Varela, V. Skumryev, M. Varela, *Appl. Phys. Lett.* **2010**, *96*, 112508.
[32] A. Tanskanen, O. Mustonen, M. Karppinen, *APL Mater.* **2017**, *5*, 056104.
[33] H. Tokoro, A. Namai, S. I. Ohkoshi, *Dalton Trans.* **2021**, *50*, 452–459.
[34] S. Sakurai, K. Tomita, K. Hashimoto, H. Yashiro, S.-I. Ohkoshi, *J. Phys. Chem. C* **2008**, *112*, 20212–20216.
[35] E. Delahaye, R. Moulin, M. Aouadi, V. Trannoy, P. Beaunier, G. Fornasieri, A. Bleuzen, *Chem. Eur. J.* **2015**, *21*, 16906–16916.
[36] R. Moulin, E. Delahaye, A. Bordage, E. Fonda, J.-P. Baltaze, P. Beaunier, E. Rivière, G. Fornasieri, A. Bleuzen, *Eur. J. Inorg. Chem.* **2017**, *Vol. 2017*, 1303–1313.
[37] J.-G. Li, G. Fornasieri, A. Bleuzen, M. Gich, A. Gloter, F. Bouquet, M. Impéror-Clerc, *Small* **2016**, *12*, 5981–5988.
[38] J.-G. Li, G. Fornasieri, A. Bleuzen, M. Gich, M. Impéror-Clerc, *ChemNanoMat* **2018**, *4*, 1168–1176.
[39] G. A. Bukhtiyarova, M. A. Shuvaeva, O. A. Bayukov, S. S. Yakushkin, O. N. Martyanov, *Nanopart. Res.* **2011**, *13*, 5527–5534.
[40] L. Kubickova, J. Kohout, P. Brazda, M. Veverka, T. Kmjec, D. Kubaniova, P. Bezdicka, M. Klementova, E. Santava, K. Zaveta, *Hyperfine Interact.* **2016**, *237*, 159.
[41] 01-079-1741 (α-Fe_2O_3); 98-005-1122 (ε-Fe_2O_3); 00-024-0081 (γ-Fe_2O_3).
[42] P. Durand, G. Fornasieri, C. Baumier, P. Beaunier, D. Durand, E. Rivière, A. Bleuzen, *J. Mater. Chem.* **2010**, *20*, 9348–9354.

[43] W. Tangwatanakul, C. Sirisathitkul, W. Limphirat, R. Yimnirun, *Chin. J. Phys.* **2017**, *55*, 845–852.
[44] M. Wilke, F. Farges, P.-E. Petit, G. E. Brown Jr., F. Martin, *Am. Mineral.* **2001**, *86*, 714–730.
[45] W. F. Brown Jr., *Phys. Rev.* **1963**, *130*, 1677–1686.
[46] M. Gich, C. Frontera, A. Roig, E. Taboada, E. Molins, H. R. Rechenberg, J. D. Ardisson, W. A. A. Macedo, C. Ritter, V. Hardy, J. Sort, V. Skumryev, J. Noguès, *Chem. Mater.* **2006**, *18*, 3889–3897.
[47] Y.-C. Tseng, N. M. Souza-Neto, D. Haskel, M. Gich, C. Frontera, A. Roig, M. van Veenendaal, J. Nogués, *Phys. Rev. B* **2009**, *79*, 094494.
[48] P. Gupta, A. Gupta, V. Franco, A. Conde, *J. Appl. Phys.* **2007**, *101*, 033909.
[49] G. V. Kurlyandskaya, J. M. Barandiaran, J. L. Munoz, J. Gutierrez, M. Vazquez, D. Garcia, V. O. Vaskovskiy, *J. Appl. Phys.* **2000**, *87*, 4822–4824.
[50] D. Cao, L. Pan, H. Li, J. Li, X. Wang, X. Cheng, Z. Wang, J. Wang, Q. Liu, *RSC Adv.* **2016**, *6*, 66795–66802.
[51] V. Briois, E. Fonda, S. Belin, L. Barthe, C. La Fontaine, F. Langlois, M. Ribbens, F. Villain, *UVX 2010 EDP Sciences* **2011**, 41–47.
[52] B. Ravel, M. Newville, *J. Synchrotron Radiat.* **2005**, *12*, 537–541.

Manuscript received: October 17, 2022
Revised manuscript received: November 22, 2022
Accepted manuscript online: November 30, 2022
Version of record online: December 15, 2022